

# Laboratory validation of lattice Boltzmann method for modeling pore-scale flow in granular materials

Muhammed E. Kutay <sup>a,1</sup>, Ahmet H. Aydilek <sup>a,\*</sup>, Eyad Masad <sup>b</sup>

<sup>a</sup> Department of Civil and Environmental Engineering, University of Maryland, 1163 Glenn Martin Hall, College Park, MD 20742, United States

<sup>b</sup> Zachry Department of Civil Engineering, Texas A&M University, 3135 TAMU, College Station, TX 77843, United States

Received 8 February 2006; received in revised form 2 July 2006; accepted 9 August 2006

Available online 23 October 2006

## Abstract

Characteristics of fluid flow through various engineering structures, such as granular filters and asphalt pavements, influence their design life. Numerical simulation of fluid flow is useful for evaluating the hydraulic characteristics of these materials. Among various techniques, the lattice Boltzmann (LB) method is widely accepted due to the ease of implementing boundary conditions and the numerical stability in a wide variety of flow conditions. It has proven to be extremely efficient in the simulation of fluid flow through the complex geometries of granular materials. In this study, two-dimensional and three-dimensional LB models were developed to represent pore-scale monophasic Newtonian incompressible fluid flow in granular materials. Three-dimensional geometries of compacted aggregates and asphalt specimens were generated from X-ray Computed Tomography technique and used as input for the LB model. The accuracy of the models was verified by comparing the results with analytical solutions of simple geometries and hydraulic conductivity measurements on the compacted aggregates and hot mix asphalt specimens. The results of LB simulations were in excellent agreement with those obtained from analytical calculations and laboratory measurements.

© 2006 Elsevier Ltd. All rights reserved.

**Keywords:** Lattice Boltzmann; Fluid flow modeling; Granular material; Hydraulic conductivity; X-ray Computed Tomography; Image processing

## 1. Introduction

Hydraulic conductivity (permeability) is one of the properties of the granular materials that has been highly correlated to their deformation, volume change, and stability behavior [24]. There are many technical difficulties with both in situ and laboratory measurements of hydraulic conductivity. Therefore, various approaches have been used to predict hydraulic conductivity based on the physical properties and microstructure distribution of granular materials. Initial attempts were concentrated on relating hydraulic conductivity to porosity, particle size distribution, and particle angularity [17,8,28,7,13]. Semi-analytical models of hydraulic conductivity were also developed where the gran-

ular microstructure was idealized as capillary networks or a regular array of spheres [13]. Derivations of these semi-analytical models are usually based on the approximation of pore structure with simpler geometries, such as tubes and cones, which are limited in capturing the complexity of pore channel shape and connectivity [8,31]. These pore structure characteristics are critical in fluid flow modeling and estimation of material hydraulic conductivity.

More recently, models have been presented to estimate hydraulic conductivity based on numerical solution of fluid flow at the material microstructural level. Adler et al. [1] solved the equations for the flow field of Newtonian fluids at low Reynolds number of isotropic artificial media that were generated based on statistical measurements made on 2-D images of the actual material. Masad et al. [23] have implemented the semi-implicit method for pressure-linked equations (SIMPLE) finite difference scheme to solve the complete set of the Navier–Stokes equations within the boundary conditions of a two-dimensional (2-D) anisotropic

\* Corresponding author. Tel.: +1 301 341 2692; fax: +1 301 405 2585.  
E-mail address: [aydilek@eng.umd.edu](mailto:aydilek@eng.umd.edu) (A.H. Aydilek).

<sup>1</sup> Turner-Fairbank Highway Research Center, FHWA, 6300 Georgetown Pike, McLean, VA 22101, United States.

## Nomenclature

|                                  |  |   |  |
|----------------------------------|--|---|--|
| $c_s$                            | lattice speed of sound   | $\mathbf{u}(\mathbf{x}, t)$                 | macroscopic velocity at node $x$ , at time $t$                           |
| $D$                              | diameter of the tube   | $u_x$                                       | velocity in the $x$ -direction   |
| $\mathbf{e}_i$                   | microscopic velocity vector (e.g. $e_1 = [1, 0]$ for D2Q9 model) | $u_y$                                       | velocity in the $y$ -direction   |
| $F_f(\mathbf{x}, t)$             | non-equilibrium distribution function at node $x$ at time $t$    | $u_z$                                       | velocity in the $z$ -direction   |
| $F_i^{\text{eq}}(\mathbf{x}, t)$ | equilibrium distribution function at node $x$ at time $t$        | $u_{z(\text{in})}$                          | velocity in $z$ -direction at the inlet nodes                            |
| $k_{zz}$                         | hydraulic conductivity in $z$ -direction                         | $u_{z(\text{out})}$                         | velocity in $z$ -direction at the outlet nodes                           |
| $n_{\text{eff}}$                 | effective porosity   | $\mathbf{x}$                                | vector coordinates of the fluid molecule                                 |
| $N_x$                            | horizontal number of lattice sites                               | $w_i$                                       | weight factor for each direction around a node                           |
| $N_y$                            | vertical number of lattice sites                                 | $\varepsilon\%$                             | percent error  |
| $P$                              | pressure   | $\Delta x, \Delta y, \text{ and } \Delta z$ | image (or lattice) resolution in $x, y$ and $z$ directions, respectively |
| $r$                              | distance from the centerline of the tube in radial direction     | $\gamma$                                    | unit weight of water   |
| RMS                              | root mean square error   | $\nabla \mathbf{p}$                         | pressure gradient  |
| $Q$                              | number of microscopic velocity vectors                           | $\nabla P_z$                                | pressure gradient in $z$ -direction                                      |
| $\mathbf{U}(\mathbf{x}, t)$      | momentum of particles at node $x$ , at time $t$                  | $\mu$                                       | dynamic viscosity  |
|                                  |  | $\nu$                                       | kinematic viscosity  |
|                                  |  | $\rho(\mathbf{x}, t)$                       | density at node $x$ , at time $t$  |
|                                  |  | $\tau$                                      | relaxation time  |

material microstructure. Al-Omari and Masad [5] utilized the same numerical scheme for modeling flow within the three dimensional (3-D) pore structure of asphalt specimens. The main advantage of these numerical models is that they introduce the effect of the microstructure distribution directly to the solution of the flow equations. They also provide detailed information about the fluid flow field within the material microstructure.

Significant progress has been made in the area of computational fluid dynamics in recent years and one of the most reliable methods, the lattice Boltzmann (LB) approach, has been increasingly used in various engineering applications to model the flow of mono and multiphase fluids [27,11,16,9,29,14]. Conventional simulations of fluid flow using numerical techniques such as finite difference, finite element, finite volume, and spectral methods generally start from the nonlinear partial differential equations (i.e., Navier–Stokes equations). These equations are discretized and solved numerically in each finite element. This approach is referred to as a ‘top-down’ approach [32]. The LB method, however, utilizes a ‘bottom-up’ approach where it reaches to the solution of Navier–Stokes equations as it evolves in the discrete (lattice) space. This evolution can be demonstrated by performing a Chapman–Enskog expansion [10]. There are several advantages of the LB method over traditional Navier–Stokes solvers. For example, Navier–Stokes solvers inevitably need to treat the nonlinear convective term; however, the convection is handled in LB through a simple uniform data shift which ultimately decreases the computational complexity significantly [33]. Furthermore, some of the Navier–Stokes solvers obtain the pressure values by solving the Poisson equation, and this operation requires global data communication and

leads to large computational cost. On the other hand, data communication is always local and pressure is computed through the equation of state in the LB method [33].

The LB method has several advantages such as ease of implementation of boundary conditions and computational efficiency through parallel computing. The method naturally accommodates some of the boundary conditions such as a pressure drop across the interface between two fluids and wetting effects at the fluid–solid interface [22]. It was proven to be very accurate in simulating isothermal, incompressible flow at low Reynolds numbers [29]; however, its application in the analysis of moisture transport through civil engineering materials, such as granular materials and hot mix asphalt, has been limited.

In this study, two-dimensional and three-dimensional numerical models were developed using the LB technique. These models were used to simulate fluid flow in simple as well as complex geometries, including the pore-scale monophasic flow of Newtonian incompressible fluid through porous granular materials and asphalt specimens. X-ray Computed Tomography (CT) was used to acquire real three-dimensional pore structures of the granular and asphalt specimens, which eliminated the errors associated with assuming idealized pore structures. The accuracy of the models was verified by comparing the results to well-known analytical solutions and laboratory measurements under controlled boundary conditions.

## 2. Background on lattice Boltzmann method

The LB method approximates the continuous Boltzmann equation by discretizing a physical space with lattice nodes and a velocity space by a set of microscopic velocity

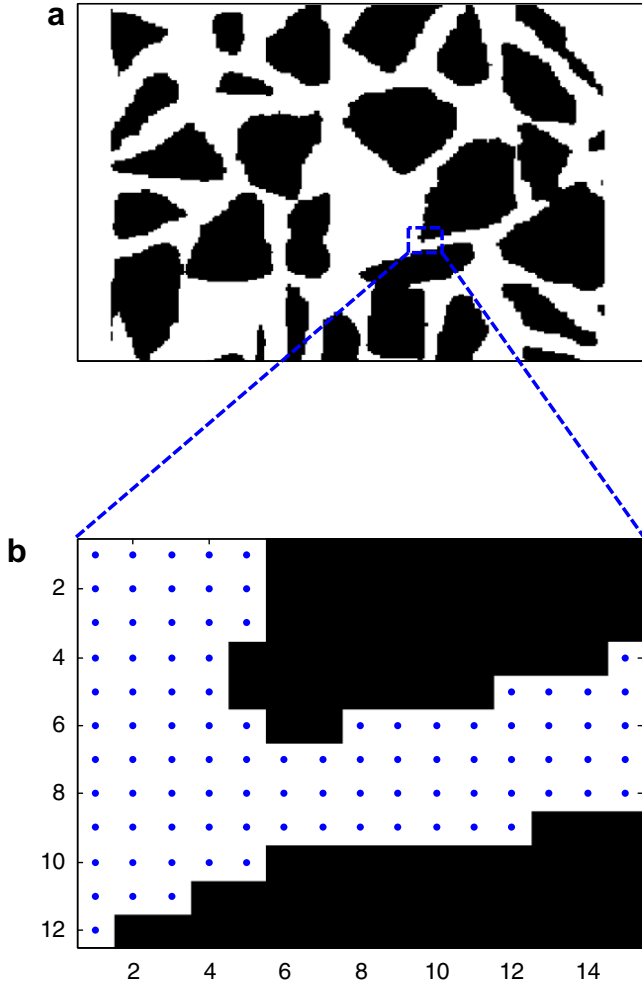


Fig. 1. (a) A binary image of aggregates, the black and white areas show the aggregates and the pores, respectively, and (b) generation of lattice nodes within the pore area of interest.

vectors [25,21]. The lattice nodes are uniformly spaced in order to represent the voids and the solids (Fig. 1), while the discrete set of microscopic velocities is defined for propagation of fluid molecules (Fig. 2). The time- and space-averaged microscopic movements of particles are modeled using molecular populations called the distribution function, which defines the density and velocity at each lattice node. Specific particle interaction rules are set so that the Navier–Stokes equations are satisfied. The time dependent movement of fluid particles at each lattice node satisfies the following particle propagation equation:

$$F_i(\mathbf{x} + \mathbf{e}_i, t + 1) = F_i(\mathbf{x}, t) - \frac{1}{\tau} [F_i(\mathbf{x}, t) - F_i^{\text{eq}}(\mathbf{x}, t)] \quad (1)$$

where  $F_i$  is the non-equilibrium distribution function,  $F_i^{\text{eq}}$  is the equilibrium distribution function, and  $\mathbf{e}_i$  is the microscopic velocity at lattice node  $\mathbf{x}$  at time  $t$ , respectively, and  $\tau$  is the relaxation time which is a function of fluid viscosity (i.e.,  $v = c_s^2(\tau - 0.5)$ ). The subscript  $i$  represents the lattice directions around the node as shown in Fig. 2. Equilibrium distribution functions for different models were derived by He and Luo [15]. The function is given in the

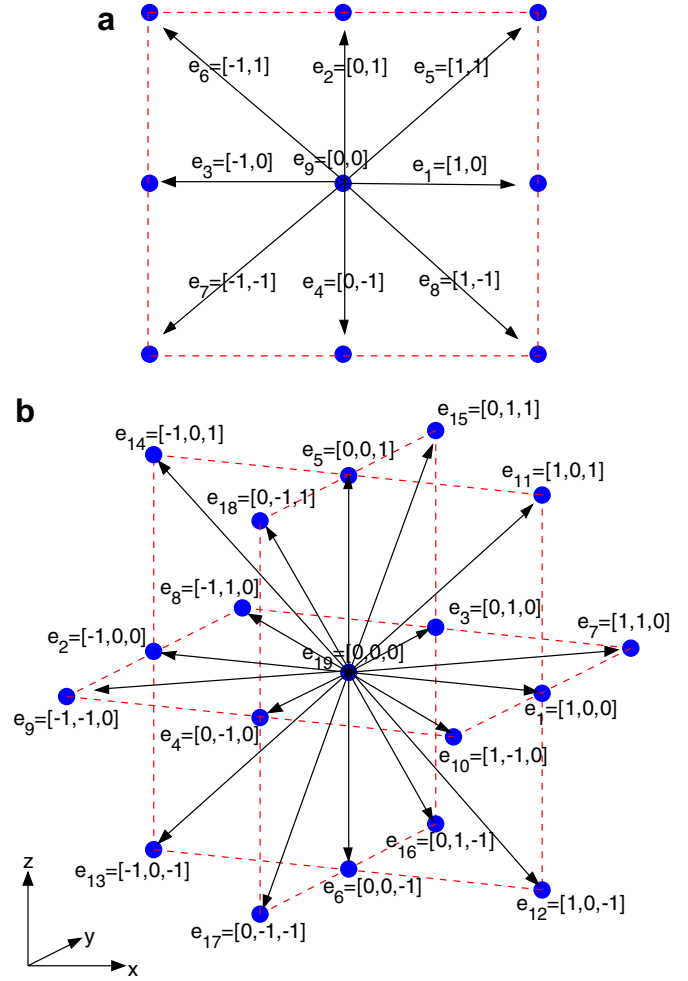


Fig. 2. (a) D2Q9, and (b) D3Q19 lattice velocity directions.

following form for the two-dimensional model with nine microscopic velocity vectors (D2Q9) and three dimensional model with nineteen microscopic velocity vectors (D3Q19):

$$F_i^{\text{eq}} = w_i \rho \left[ 1 + 3(\mathbf{e}_i \cdot \mathbf{u}) + \frac{9}{2}(\mathbf{e}_i \cdot \mathbf{u})^2 - \frac{3}{2}(\mathbf{u} \cdot \mathbf{u}) \right] \quad (2)$$

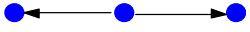
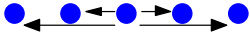
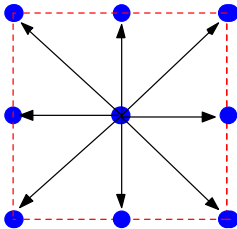
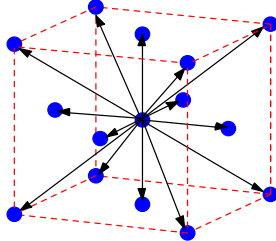
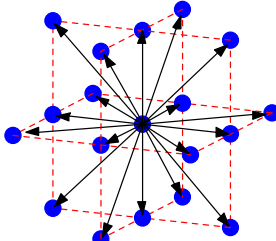
where  $\rho$  is the density of the node, and  $w_i$  is the weight factor in the  $i$ th direction. Weight factors vary for different LB models, as listed in Table 1. For instance, the weight factors ( $w_i$ ) for the D2Q9 LB model are:  $w_0 = 16/36$  for rest particle,  $w_i = 4/36$  ( $1 \leq i \leq 4$ ) for particles streaming to the face-connected neighbors and  $w_i = 1/36$  ( $5 \leq i \leq 8$ ) for particles streaming to the edge-connected neighbors. The weight factors are derived based on the lattice type (DxQy) and the derivations can be found in Wolf-Gladrov [32].

The macroscopic properties, density ( $\rho$ ), momentum ( $\mathbf{U}$ ), and velocity ( $\mathbf{u}$ ) of the nodes are calculated using the following relations:

$$\rho = \sum_{i=1}^Q F_i \quad (3)$$

$$\mathbf{U} = \sum_{i=1}^Q [F_i \mathbf{e}_i] \quad (4)$$

Table 1  
Properties of commonly implemented lattice Boltzmann models

| Model name | Lattice speed of sound, ( $c_s^2$ ) | Weight factors                                | Velocity directions   |
|------------|-------------------------------------|---|---|
| D1Q3       | 1/3                                 | $4/6^{(1)}$<br>$1/6^{(2)}$                    |    |
| D1Q5       | 1                                   | $6/12^{(1)}$<br>$2/12^{(2)}$<br>$1/12^{(2)}$  |    |
| D2Q9       | 1/3                                 | $16/36^{(1)}$<br>$4/36^{(2)}$<br>$1/36^{(3)}$ |    |
| D3Q15      | 1/3                                 | $16/72^{(1)}$<br>$8/72^{(2)}$<br>$1/72^{(3)}$ |   |
| D3Q19      | 1/3                                 | $12/36^{(1)}$<br>$2/36^{(2)}$<br>$1/36^{(3)}$ |  |

Note: Weight factors for <sup>(1)</sup> rest particle, <sup>(2)</sup> face-connected neighbors, and <sup>(3)</sup> edge-connected neighbors.

$$\mathbf{u} = \frac{\mathbf{U}}{\rho} \quad (5)$$

where  $Q$  is the number of microscopic velocity vectors connected to node  $i$ .

### 3. Implementation of the lattice Boltzmann method

The LB algorithm developed in this study consists of three major phases. Fig. 3 provides the flowchart of this algorithm. The initial conditions of the simulation are set in the first phase. In the second phase, the propagation of the distribution function to the neighboring nodes and the collision process are performed. Then, the new density and macroscopic velocity of each node for the next time step is computed. The third phase involves assigning boundary conditions and the calculation of new equilibrium distribution functions.

#### 3.1. Phase I – Initialization

In the first phase, densities and velocities of the lattice nodes are set to an initial value and initial equilibrium distribution functions at all nodes are calculated using Eq. (1). To increase the computational efficiency, the relaxation time ( $\tau$ ) is set to unity and, as a result, Eq. (1) is simplified to the following form:

$$F_i(\mathbf{x} + \mathbf{e}_i, t + 1) = F_i^{\text{eq}}(\mathbf{x}, t) \quad (6)$$

The non-equilibrium distribution function ( $F_i$ ) is initially set to be equal to the equilibrium distribution function.

#### 3.2. Phase II – Propagation to the neighboring nodes and boundary conditions

Fig. 4a shows the orientation of the equilibrium distribution function components at time  $t$  ( $F_i^{\text{eq}}(\mathbf{x}, t)$ ), where each component points towards the direction of a microscopic velocity vector ( $\mathbf{e}_i$ ). The components at each node propagate to the neighboring nodes and produce the non-equilibrium distribution function for the next time step of the neighboring node ( $F_i(\mathbf{x} + \mathbf{e}_i, t + 1)$ ). The propagation is performed using Eq. (1).

Fig. 4b illustrates migration of distribution function components from the neighboring nodes (both  $F_i$  and  $F_i^{\text{eq}}$ ) and orientation of non-equilibrium distribution function components ( $F_i$ ) of the current node. Note that  $F_i^*$  in Fig. 4b represents both non-equilibrium and equilibrium distribution function components. After colliding at a node, these components define the density and momentum of that particular node through Eqs. (3) and (4), respectively.

##### 3.2.1. Boundary conditions at solid nodes

In the particle propagation step of the algorithm, all components of the non-equilibrium distribution function are computed at each node except at nodes that are neighbors with solid nodes. Fig. 5 demonstrates the solid and pore nodes in an aggregate structure. At those neighboring nodes, certain components of the distribution function that are expected to be migrating from the solid node are unknown. In this case, a wall boundary condition is used to calculate the missing components. The most commonly used technique to calculate unknown components of the distribution function at these nodes is the application of no-slip boundary condition [20]. It is also referred to as the *bounce-back* scheme, in which the distribution function components heading towards the solid nodes scatter directly back to the node. Two kinds of no-slip boundary conditions exist. The first one, named as *full bounce-back*, assumes that the wall is located at the solid nodes whereas the second one, named as *half-way bounce-back*, assumes that the wall is located half-way between the pore and solid nodes. The solid and dashed lines in Fig. 5 show the wall boundaries for full bounce-back and half-way bounce-back scheme, respectively. It has been shown that a full

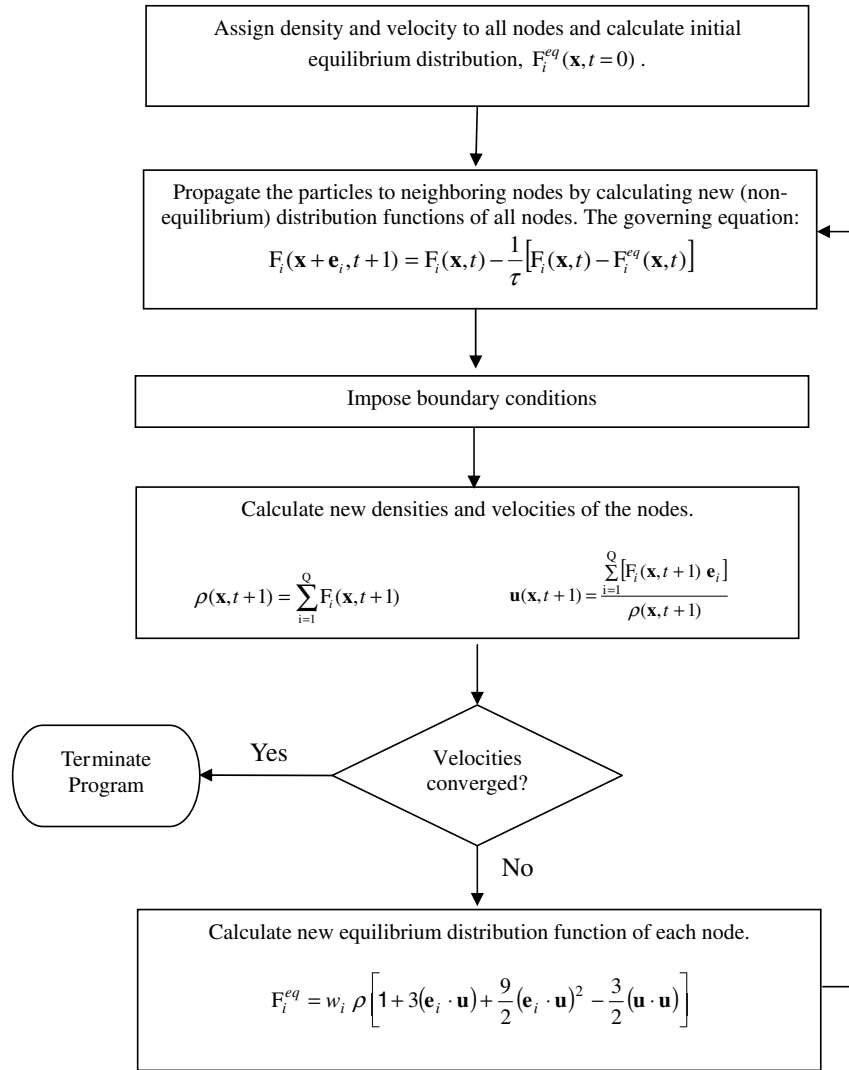


Fig. 3. Flow chart of the LB algorithm.

bounce-back provides first-order accuracy, whereas a half-way bounce-back provides second-order accuracy [34]. The latter was used in the current simulations to calculate the missing components of the distribution function at nodes that are neighbors of solid nodes.

### 3.2.2. Boundary conditions at domain boundaries in D2Q9 and D3Q19 Models

In addition to nodes that are neighbors of solid nodes, certain components of the distribution function of the nodes located at the boundaries of the domain (i.e., inlet, outlet, top and bottom nodes, as seen in Fig. 5) are also unknown. These components (e.g.,  $F_1$ ,  $F_5$ , and  $F_8$  at the inlet nodes) are calculated from the known components (e.g.,  $F_2$ ,  $F_4$ ,  $F_3$ ,  $F_6$ ,  $F_7$  and  $F_9$  at the inlet nodes) and by setting two constraints, such as prescribing two components of macroscopic velocity (i.e.,  $u_x$ ,  $u_y$ ). Another set of alternative constraints can be the density and one component of the macroscopic velocity (i.e.,  $\rho$ ,  $u_x$ ) at those nodes. Given

the two components of the macroscopic velocity, the density and unknown distribution function components at those nodes are calculated using the relationships provided in Table 2. These relationships are based on the density and momentum equations (Eqs. (3) and (4), respectively). The unknown components of the distribution function given in Table 2 are calculated by assuming that the half-way bounce-back scheme is valid for the non-equilibrium part of the particle distribution function as described by Zou and He [35].

In a three-dimensional cubical lattice space (D3Q19), the computation of unknown distribution function components in all six faces of the domain is difficult. At least two components of the macroscopic velocity and density, or all three components of the macroscopic velocity vector need to be known at these domain boundaries. Since the cylindrical specimens tested in the laboratory in the current study were confined by a membrane (i.e., solid wall), only the unknown distribution functions at the inlet and the



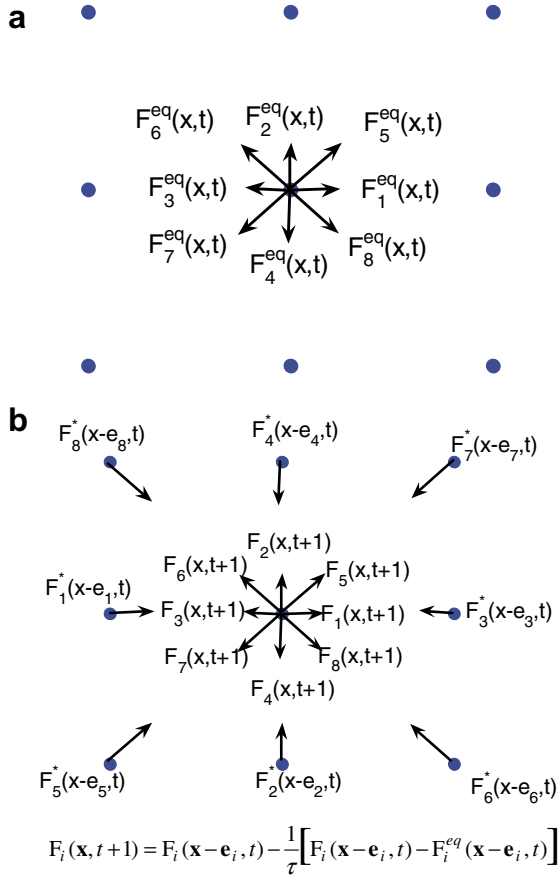


Fig. 4. (a) Orientation of components of equilibrium distribution function calculated in the current time step, and (b) illustration of migration of distribution function components from the neighboring nodes. Note that  $F_i^*$  represents both non-equilibrium and equilibrium distribution function components.

outlet were of interest. It should be noted that the relations given in Table 3 were derived based on the constraints that the pressure gradient acts in  $z$ -direction only, velocity parallel to the inlet and outlet face are zero (i.e.,  $u_x = 0$  and  $u_y = 0$ ), and density at these nodes are known. Considering a linear relationship between density and pressure in lattice space ( $P = c_s^2 \rho$ , where  $P$  is pressure,  $\rho$  is density and  $c_s$  is the lattice speed of sound), densities at the inlet and outlet were set to create flow from high-density (high pressure) inlet nodes towards low-density (low pressure) outlet nodes [21].

### 3.3. Phase III – New equilibrium distribution functions

In this part of the algorithm, macroscopic flow variables (i.e., density and velocity) and the new values of the equilibrium distribution function are computed for each lattice node at time step  $t + 1$ . Phases II and III are repeated until the difference in average velocities of the domain calculated in the previous time and current time steps is less than a threshold value, which confirms the onset of steady-state flow.

## 4. Verification of the D2Q9 Model

Wannier [30] has provided a closed form analytical solution for Stokes flow around a cylinder in the vicinity of a moving plate. In order to confirm the accuracy of the D2Q9 model, comparisons were made between the D2Q9 model results and the predictions of the Wannier [30] analytical solution. A cylinder with a diameter of 20 mm was placed with its center 35 mm from a moving plate, as shown in Fig. 6a. Streamlines and velocity vectors were calculated from the analytical equation given by Wannier [30] for a 70 mm by 70 mm window. Herein, a streamline is defined as a line that is tangent to the velocity vectors everywhere in space. Simulations were carried out with a varying number of lattice nodes:  $70 \times 70$ ,  $140 \times 140$ , and  $280 \times 280$ , to demonstrate the accuracy of the LB model. A velocity of  $u_x = 10^{-7}$  mm/s was prescribed at the bottom boundary. Missing components of the distribution function at the boundaries were calculated using the relationships given in Table 2.

Fig. 6a compares the streamlines computed from the LB simulations using  $280 \times 280$  lattice resolution with the streamlines computed from the Wannier [30] analytical equation. The results clearly indicate that an excellent agreement exists between the analytical solution and the LB-based results, which confirms the validity of the D2Q9 model for predicting a well-known analytical solution. To investigate the order of accuracy for the LB model, the root mean square (RMS) of error was calculated for three lattice resolutions (i.e.,  $N_x * N_y$ , the horizontal times vertical number of lattice sites, varied from 1 to 3). As seen in Fig. 6b, the RMS ranges from  $4 \times 10^{-12}$  to  $2 \times 10^{-10}$  and decreases with increasing resolution (number of lattice nodes). Fig. 6b also shows that the RMS decreases approximately four times as the number of lattice sites doubled, which suggests a second-order accuracy of the D2Q9 model implemented in this study.

## 5. Verification of the D3Q19 Model

The velocity distribution of laminar flow through a single circular tube with diameter  $D$  can be calculated using Poiseuille's Law as follows:

$$u_z = \frac{\nabla P_z}{\mu} \left( \frac{D^2}{16} - \frac{r^2}{4} \right) \quad (7)$$

where  $u_z$  is the velocity in the vertical direction ( $z$ -direction),  $\nabla P_z$  is the pressure gradient,  $\mu$  is the dynamic viscosity,  $D$  is the tube diameter, and  $r$  is the distance from the centerline of the tube in radial direction. Flow through a 10-mm diameter circular tube was simulated using the D3Q19 LB model. A pressure gradient of  $10^{-6}$  g/mm<sup>2</sup> s<sup>2</sup> was applied to the system to trigger the flow. Velocity values at the inlet and outlet were computed using the equations provided in Table 3. Simulations were carried out at three different resolutions: 10, 20, and 40 lattice points

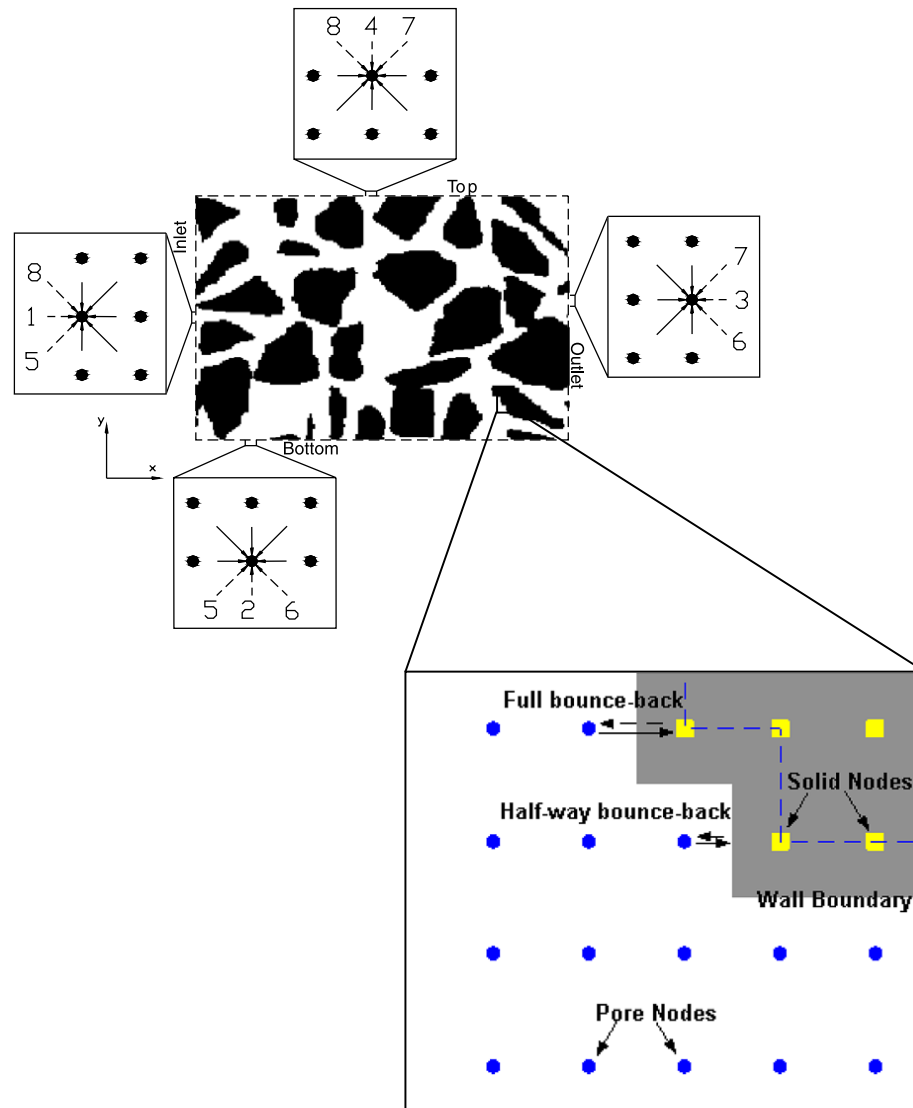


Fig. 5. Illustration of unknown components of the distribution function streaming from outside of the boundaries and full bounce back and half-way bounce back boundary conditions near solid nodes.

Table 2

Relations for the unknowns at the boundaries for D2Q9 model

| Boundary nodes | Known components                         | Unknown components    | Relations  |
|----------------|--|-----------------------|--|
| Inlet          | $u_x, u_y, F_9, F_2, F_4, F_3, F_6, F_7$ | $\rho, F_1, F_8, F_5$ | $\rho_{in} = \frac{1}{1-u_{x(in)}} [F_9 + F_2 + F_4 + 2(F_3 + F_6 + F_7)]$ $F_1 = F_3 + \frac{2}{3}\rho u_x$ $F_8 = F_6 + \frac{1}{2}(F_2 - F_4) + \frac{1}{6}\rho u_x - \frac{1}{2}\rho u_y$ $F_5 = F_7 - \frac{1}{2}(F_2 - F_4) + \frac{1}{6}\rho u_x + \frac{1}{2}\rho u_y$         |
| Outlet         | $u_x, u_y, F_9, F_2, F_4, F_1, F_5, F_8$ | $\rho, F_3, F_6, F_7$ | $\rho_{out} = \frac{1}{1-u_{x(out)}} [F_9 + F_2 + F_4 + 2(F_3 + F_6 + F_7)]$ $F_3 = F_1 - \frac{2}{3}\rho u_x$ $F_6 = F_8 - \frac{1}{2}(F_2 - F_4) - \frac{1}{6}\rho u_x + \frac{1}{2}\rho u_y$ $F_7 = F_5 + \frac{1}{2}(F_2 - F_4) - \frac{1}{6}\rho u_x - \frac{1}{2}\rho u_y$       |
| Bottom         | $u_x, u_y, F_9, F_1, F_3, F_4, F_7, F_8$ | $\rho, F_2, F_6, F_5$ | $\rho_{bottom} = \frac{1}{1-u_{y(bottom)}} [F_9 + F_1 + F_3 + 2(F_4 + F_7 + F_8)]$ $F_2 = F_4 + \frac{2}{3}\rho u_y$ $F_6 = F_8 + \frac{1}{2}(F_1 - F_3) + \frac{1}{6}\rho u_y - \frac{1}{2}\rho u_x$ $F_5 = F_7 - \frac{1}{2}(F_1 - F_3) + \frac{1}{6}\rho u_y + \frac{1}{2}\rho u_x$ |
| Top            | $u_x, u_y, F_9, F_1, F_3, F_2, F_6, F_5$ | $\rho, F_4, F_7, F_8$ | $\rho_{top} = \frac{1}{1-u_{y(top)}} [F_9 + F_1 + F_3 + 2(F_2 + F_6 + F_5)]$ $F_4 = F_2 - \frac{2}{3}\rho u_y$ $F_8 = F_6 - \frac{1}{2}(F_1 - F_3) - \frac{1}{6}\rho u_y + \frac{1}{2}\rho u_x$ $F_7 = F_5 + \frac{1}{2}(F_1 - F_3) - \frac{1}{6}\rho u_y - \frac{1}{2}\rho u_x$       |

Table 3  
Relations for the unknowns at the boundaries for 3Q19 model

| Boundary nodes | Known components   | Unknown components                         | Relations  |
|----------------|--|--|--|
| Inlet          | $\rho, u_x = 0, u_y = 0, F_{19}, F_1, F_2, F_3, F_4, F_6, F_7, F_8, F_9, F_{10}, F_{12}, F_{13}, F_{16}, F_{17}$ | $u_z, F_5, F_{11}, F_{14}, F_{15}, F_{18}$ | $u_{z(in)} = 1 - \frac{F_{19} + \sum_{i=1}^4 F_i + \sum_{i=7}^{10} F_i + 2(F_6 + F_{12} + F_{13} + F_{16} + I)}{\rho_{in}}$ $F_5 = F_6 + \frac{1}{3}\rho u_z$ $F_{15} = F_{17} - \frac{1}{4}(F_3 - F_4) + \frac{1}{6}\rho u_z$ $F_{18} = F_{16} + \frac{1}{4}(F_3 - F_4) + \frac{1}{6}\rho u_z$ $F_{11} = F_{13} - \frac{1}{4}(F_1 - F_2) + \frac{1}{6}\rho u_z$ $F_{14} = F_{12} + \frac{1}{4}(F_1 - F_2) + \frac{1}{6}\rho u_z$    |
| Outlet         | $\rho, u_x = 0, u_y = 0, F_{19}, F_1, F_2, F_3, F_4, F_7, F_8, F_9, F_{10}, F_5, F_{11}, F_{14}, F_{15}, F_{18}$ | $u_z, F_6, F_{12}, F_{13}, F_{16}, F_{17}$ | $u_{z(out)} = -1 + \frac{F_{19} + \sum_{i=1}^4 F_i + \sum_{i=7}^{10} F_i + 2(F_5 + F_{11} + F_{14} + F_{15} + I)}{\rho_{out}}$ $F_6 = F_5 - \frac{1}{3}\rho u_z$ $F_{17} = F_{15} + \frac{1}{4}(F_3 - F_4) - \frac{1}{6}\rho u_z$ $F_{16} = F_{18} - \frac{1}{4}(F_3 - F_4) - \frac{1}{6}\rho u_z$ $F_{13} = F_{11} + \frac{1}{4}(F_1 - F_2) - \frac{1}{6}\rho u_z$ $F_{12} = F_{14} - \frac{1}{4}(F_1 - F_2) - \frac{1}{6}\rho u_z$ |

along the diameter. Fig. 7a shows the velocity profiles computed using Eq. (7) and the velocities based on the LB simulations. An excellent agreement exists between the results based on Poiseuille's Law and the D3Q19 model. As seen in Fig. 7b, the RMS of error is quite low; ranges from  $5 \times 10^{-6}$  to  $7.5 \times 10^{-5}$ , and decreases with an increase in

resolution (number of lattice nodes). A line representing 2:1 slope included in Fig. 7b suggests the second order accuracy of the D3Q19 model. These comparisons confirm

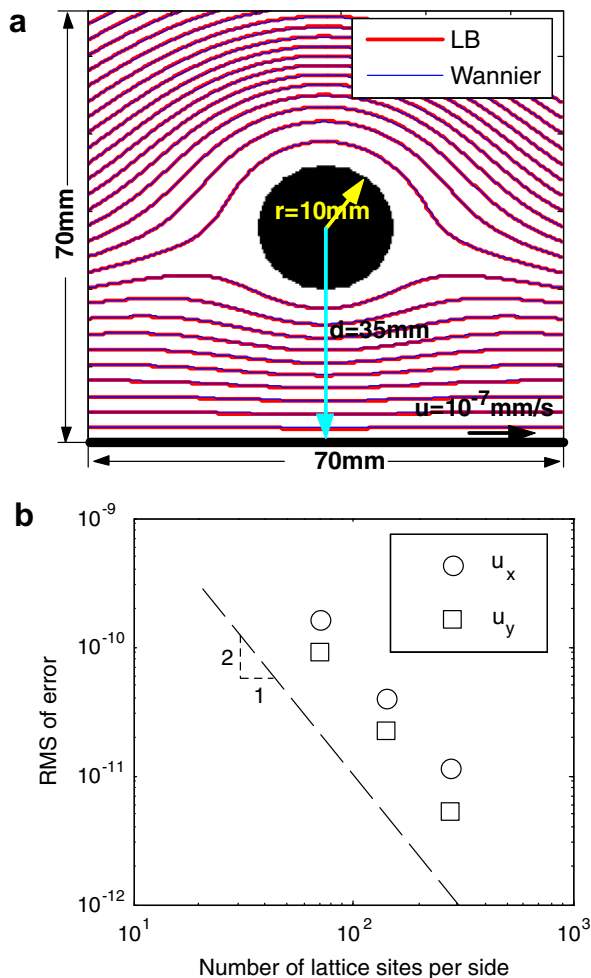


Fig. 6. (a) Streamlines computed by the LB simulation and analytical solution, (b) RMS of error in vertical velocity ( $u_y$ ), and horizontal velocity ( $u_x$ ).

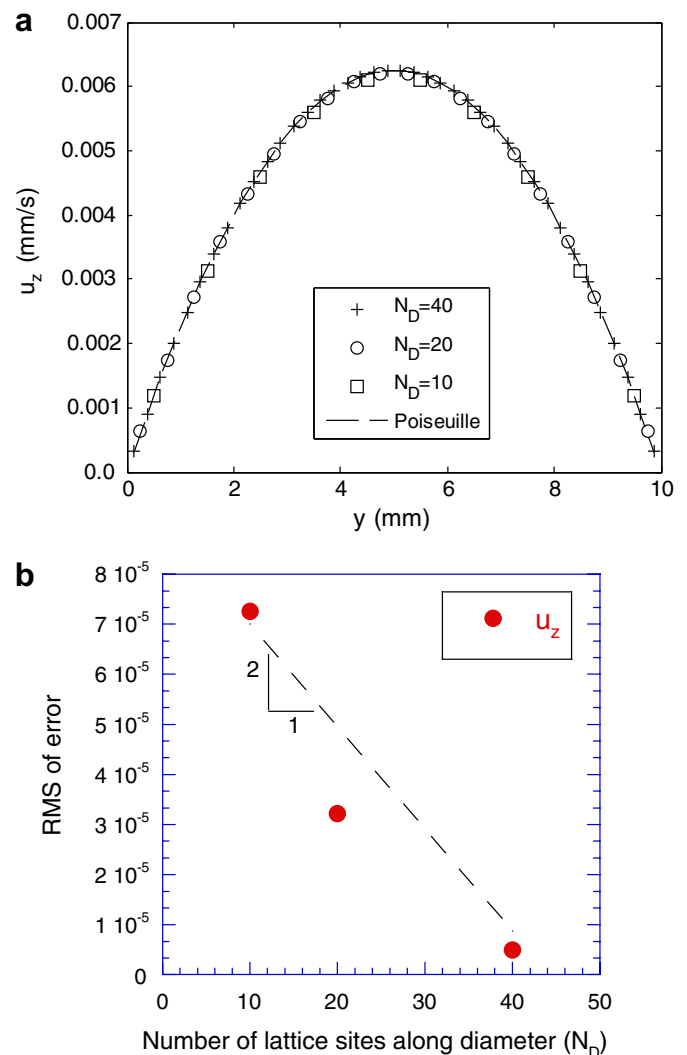


Fig. 7. (a) Effect of lattice points along the diameter on velocity profiles of flow in a circular tube, and (b) RMS of error in  $u_z$  between the analytical solution and LB simulation.



the accuracy of the D3Q19 LB model for predicting the three-dimensional flow field.

## 6. Laboratory validation of the D3Q19 LB Model

### 6.1. Materials and laboratory methods

A series of laboratory hydraulic conductivity tests were conducted on compacted aggregates and asphalt specimens to further confirm the validity of the D3Q19 LB model in simulating three-dimensional flow. Specimens were compacted using aggregates with average equivalent diameters retained on 9.5 mm, 4.75 mm, and 2.36 mm sieves. These specimens were labeled as AG1, AG2, and AG3, respectively. The aggregates were placed in specially fabricated molds of 100 mm in diameter and 130 mm in height. The molded specimens were tapped from two sides to a unit weight of  $18.1 \text{ kN/m}^3$ , and subjected to hydraulic conductivity tests using the constant head method in accordance with ASTM D 2434.

Asphalt specimens used in this study included 8 Superpave mixtures and 12 SMA (Stone Matrix Asphalt) mixtures. The properties of these types of mixtures are available in Roberts et al. [26]. In general, the Superpave mixtures are continuously graded, while the SMA mixtures are gap-graded. Table 4 presents the mix design properties of the asphalt specimens tested in this study. As indicated in this table, the mixtures differed in their gradations and porosities. The term Nominal Maximum Aggregate Size (NMAS) refers to the largest sieve that retains less than 10% of the aggregates. The bulk specific gravity was measured following the procedure summarized in AASHTO T 166 [3]. The maximum specific gravity ( $G_{\text{mm}}$ ) refers to

the specific gravity of the mixture with no voids, and it was measured using AASHTO T 209 [4]. The number of gyrations refers to the compaction effort applied in the gyratory compactor to achieve different porosities [26].

The vertical hydraulic conductivities ( $k_{zz}$ ) of the specimens were determined using a bubble tube flexible-wall constant head permeameter that was specially designed for measuring the hydraulic conductivity of asphalt specimens of 150 mm in diameter and 70 mm in height [18].

### 6.2. Image acquisition and generation of lattice nodes

The first input needed for the fluid flow simulation using the LB method was the 3D geometry of the specimens, which was generated using the X-ray Computer Tomography (CT) technique. The X-ray CT is a powerful non-destructive imaging technique that captures the interior structure of materials using their X-ray attenuation characteristics. Two-dimensional image slices of the specimens were captured using the X-ray CT device and the slices were stacked to reconstruct the 3D structure. The vertical resolution ( $\Delta z$ ) of the two-dimensional grayscale images was registered by the aperture of the linear detector of the X-ray CT device, which was 0.8 mm. The horizontal resolutions, on the other hand, were directly related to the specimen diameter. A uniform resolution of 0.4–0.8 mm/pixel was achieved in all directions ( $x$ ,  $y$  and  $z$ ) by resizing the image slices using bilinear interpolation [19].

The captured images were converted into a binary form (black and white) by using a threshold pixel intensity, where black areas (pixel values of 0) represent solid particles and white areas (pixel values of 1) represent air voids. The threshold value can have a crucial effect on the correct

Table 4  
Properties of the asphalt specimens tested

| Specimen ID | NMAS (mm) | N. Gyr. | Gradation | $P_b$ (%) | $G_{\text{mm}}$ (g/cm <sup>3</sup> ) | $G_{\text{mb}}$ (g/cm <sup>3</sup> ) | $n$ (%) |
|-------------|-----------|---------|-----------|-----------|--------------------------------------|--------------------------------------|---------|
| 9.5C25      | 9.5       | 25      | SP/Coarse | 4.76      | 2.72                                 | 2.42                                 | 10.9    |
| 12.5C25     | 12.5      | 25      | SP/Coarse | 5.32      | 2.71                                 | 2.55                                 | 5.8     |
| 19F25       | 19        | 25      | SP/Fine   | 4.51      | 2.74                                 | 2.52                                 | 8.1     |
| 19C25       | 19        | 25      | SP/Coarse | 4.85      | 2.74                                 | 2.43                                 | 11.4    |
| 25F25       | 25        | 25      | SP/Fine   | 4.00      | 2.76                                 | 2.50                                 | 9.5     |
| 25C25       | 25        | 25      | SP/Coarse | 4.63      | 2.75                                 | 2.43                                 | 11.9    |
| 25C50       | 25        | 50      | SP/Coarse | 4.63      | 2.75                                 | 2.50                                 | 9.4     |
| 25C75       | 25        | 75      | SP/Coarse | 4.63      | 2.75                                 | 2.48                                 | 9.9     |
| 9.5SMA-A1   | 9.5       | 50      | SMA       | 5.50      | 2.72                                 | 2.32                                 | 14.7    |
| 9.5SMA-A2   | 9.5       | 50      | SMA       | 5.50      | 2.72                                 | 2.28                                 | 16.3    |
| 9.5SMA-B1   | 9.5       | 25      | SMA       | 5.50      | 2.72                                 | 2.13                                 | 21.6    |
| 9.5SMA-B2   | 9.5       | 25      | SMA       | 5.50      | 2.72                                 | 2.26                                 | 16.8    |
| 12.5SMA-A1  | 12.5      | 75      | SMA       | 5.50      | 2.71                                 | 2.27                                 | 16.2    |
| 12.5SMA-A2  | 12.5      | 75      | SMA       | 5.50      | 2.71                                 | 2.10                                 | 22.4    |
| 12.5SMA-B1  | 12.5      | 50      | SMA       | 5.50      | 2.71                                 | 2.37                                 | 12.5    |
| 12.5SMA-B2  | 12.5      | 50      | SMA       | 5.50      | 2.71                                 | 2.21                                 | 18.5    |
| 19SMA-A1    | 19        | 25      | SMA       | 5.50      | 2.74                                 | 2.34                                 | 14.7    |
| 19SMA-A2    | 19        | 25      | SMA       | 5.50      | 2.74                                 | 2.29                                 | 16.6    |
| 19SMA-B1    | 19        | 75      | SMA       | 5.50      | 2.74                                 | 2.36                                 | 14.0    |
| 19SMA-B2    | 19        | 75      | SMA       | 5.50      | 2.74                                 | 2.24                                 | 18.1    |

Note:  $P_b$  = Opt. binder content;  $G_{\text{mm}}$  = Maximum specific gravity of the mix;  $G_{\text{mb}}$  = Bulk specific gravity of the mix; N. Gyr. = Number of gyrations; NMAS = Nominal maximum aggregate size;  $n$  = Porosity; SP = Superpave mixture; SMA = Stone matrix asphalt.

determination of the pore structure and measured quantities as discussed below. Following the generation of binary images, an additional task was performed to increase the speed of the simulations. An algorithm was developed to eliminate the isolated pores that had no connection to any of the outside boundaries (i.e., surface) of the specimen, and lattice nodes were generated only at the centers

of each white voxel (three-dimensional pixel) that represented the interconnected pore spaces. It is important to mention that this step was not required for the LB simulations; however, the isolated pores were eliminated solely to speed up the simulation at each time step. Furthermore, decreasing the number of nodes reduced the total number of time steps to reach the steady state flow condition. Examples of 3D images of aggregates and asphalt specimens are provided in Fig. 8. More detailed discussion on the X-ray CT technique, specifications of the device utilized in this study, and the methods followed for processing the captured images are provided by Kutay and Aydilek [19].

### 6.3. LB fluid flow simulations

#### 6.3.1. Compacted aggregates

A density (pressure) gradient in the range of  $5.34 \times 10^{-3}$ – $3.6 \times 10^{-5} \text{ g/mm}^2 \text{ s}^2$  was applied to the system to initiate the flow. The velocities and unknown components of the distribution function at the inlet and outlet nodes were calculated using the equations given in Table 3. The LB fluid flow simulations were run until steady-state flow condition was achieved. The steady-state flow criterion was set such that the difference in the overall mean velocity in the  $z$ -direction ( $u_z$ ) between two consecutive time steps was less than a threshold value. This threshold was selected as 0.001% of the mean velocity at the current time step. Fig. 9 shows the change in mean velocity over time steps during LB simulations for specimen 25C75. In this particular case, the steady state flow was observed after approximately 52,000 time steps. In general, more number of time steps was required for the system to stabilize for specimens with highly irregular pore-solid interfaces. Similar observations were also made by Duarte et al. [12] in their 2D cellular automata-based model of flow through cylindrical obstacles placed between parallel plates.

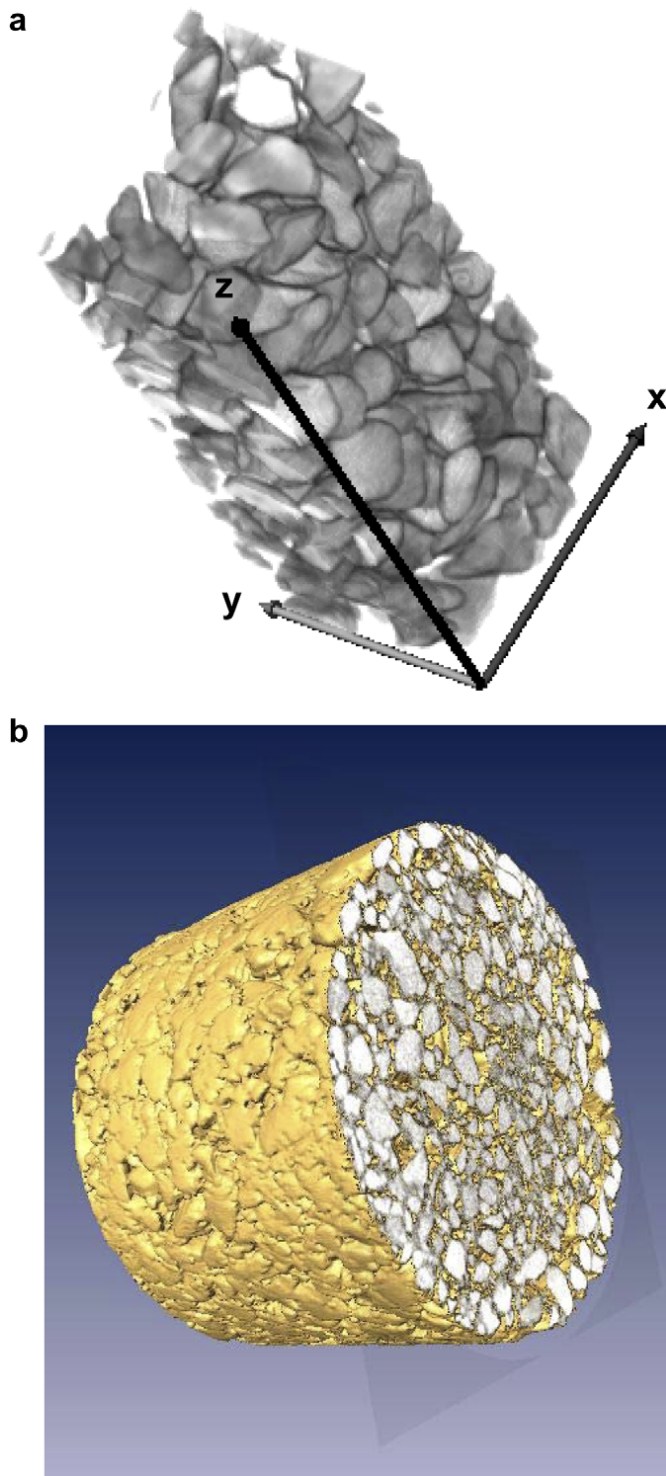


Fig. 8. 3D reconstructed X-ray CT image of (a) compacted aggregate specimen, and (b) hot mix asphalt specimen.

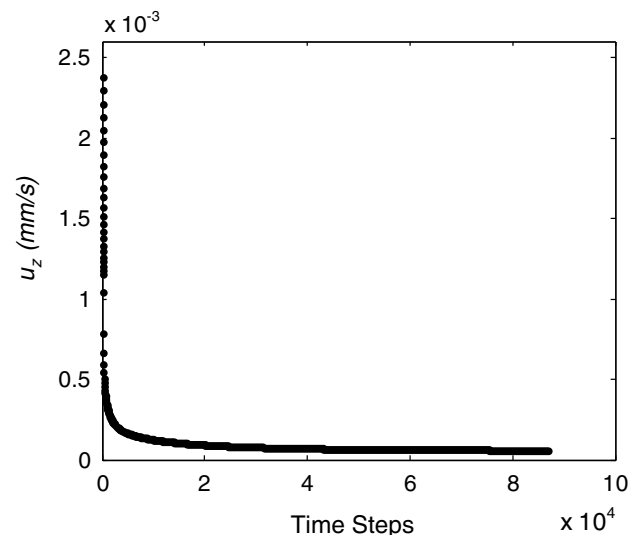


Fig. 9. Variation in mean velocity with time steps for specimen 25C75.

Following the onset of steady-state flow, vertical hydraulic conductivities were computed as follows:

$$k_{zz} = -\gamma n_{\text{eff}} (u_z / \nabla P_z) \quad (8)$$

where  $k_{zz}$  is the hydraulic conductivity in the  $z$ -direction,  $\gamma$  is the unit weight of water,  $n_{\text{eff}}$  is the effective porosity which represents the percentage of connected voids,  $u_z$  is the average velocity in the pore structure of the entire specimen in the  $z$ -direction, and  $\nabla P_z = \frac{(P_{z-\text{in}} - P_{z-\text{out}})}{L}$  is the pressure gradient in the  $z$ -direction. Fig. 10a shows the laboratory measured versus LB-simulated hydraulic conductivities of the aggregate structure. A very good agreement is obtained between the measured and simulated values. The laboratory-based hydraulic conductivities are slightly lower than those predicted by the LB model. One possibility for this difference may be attributed to the presence of air bubbles in tap water that may have blocked the

flow pathways leading to low hydraulic conductivity measurements. Aydilek and Kutay [6] showed that this phenomenon is commonly observed in testing of coarse-grained soils. Another possible reason is the difficulty of maintaining low hydraulic gradients during the laboratory tests. Since the aggregates had large pore structure, very low hydraulic gradients were needed in order to keep the flow in the laminar range as Darcy's law is valid for laminar flow only. However, the lack of specimen confinement with a membrane in the ASTM D 2434 test set-up prevented application of such low hydraulic gradients.

### 6.3.2. Asphalt specimens

Similar to the testing of aggregates, pressure (i.e., density) values were set at the inlet and the outlet of the specimen during the LB simulations to simulate the pressure boundary conditions of the laboratory bubble tube constant head hydraulic conductivity test. A pressure gradient in the range of  $8.97 \times 10^{-4} - 1 \times 10^{-3} \text{ g/mm}^2 \text{ s}^2$  was applied in order to simulate the pressure boundary conditions occurring in the laboratory test permeameter. The curved faces of the cylindrical specimens were confined by solid nodes (i.e. black pixels) to simulate a typical membrane that confines the specimen in a laboratory test. The components of the velocity vector perpendicular to the density gradient at the inlet and outlet nodes were initially set to zero (i.e., no slip boundary condition). Unknown components of the distribution function as well as the velocity in  $z$ -direction at inlet and outlet nodes were computed using the equations given in Table 3. After the steady state flow condition was achieved, vertical hydraulic conductivities were computed using Eq. (8).

Computed hydraulic conductivities based on the LB simulations are plotted against the laboratory measurements of hydraulic conductivity in Fig. 10b. The data clearly indicates that the LB-based hydraulic conductivities are in a very good agreement with the laboratory measurements. Most of the results are within the variability limits of the laboratory test as indicated by the error bars in Fig. 10b.

### 6.4. Sensitivity of the simulated hydraulic conductivities to the selected grayscale threshold value

The most important factor that influences the LB model predictions is the accuracy of representing the pore structure distribution. In the current study, the X-ray CT-generated grayscale images were converted to binary images to separate the solid phase from the pores by using a selected threshold pixel intensity. This threshold value influences the pore structure distribution. In principle, air voids (with negligible density compared to the solids) should have the lowest pixel values in the image since the grayscale intensities of the X-ray CT images are proportional to the density of the material at the location of a pixel. Consequently, a pixel intensity that is close to zero can be selected as the threshold to discriminate the pores from the solid nodes.

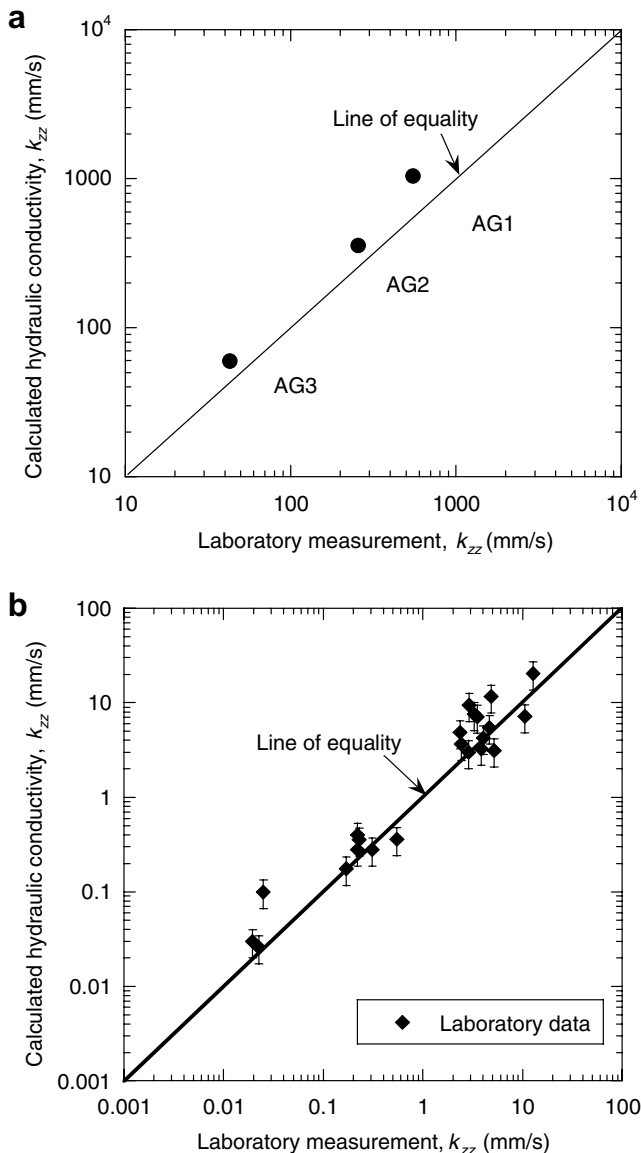


Fig. 10. Laboratory measured versus LB-computed hydraulic conductivity of (a) compacted aggregates, and (b) asphalt specimens.



However, this approach does not provide accurate results because the built-in algorithm for intensity interpolation in the X-ray CT gives different pixel intensity to pores depending on their size and the intensity of the surrounding solid phase. Small isolated pores, which are close in size to the image resolution, tend to have elevated pixel intensities compared with the large pores. Therefore, the selection of a high threshold value that captures the small pores could widen the boundaries of the larger pores in other locations.

Fig. 11 is given as an example to demonstrate this phenomenon. An increase in the threshold value from 0 to 120 pixel intensities resulted in an increase of porosity of spec-

imen 25C75 from 3.15% to 11.2%. A close examination of the images at different threshold levels reveals that small isolated pores cannot be detected at a low threshold value. Conversely, additional pores are introduced into the image when relatively high threshold values are selected. This can clearly be seen when the original image and the image obtained at a threshold value of 120 are compared. Similar observations were made on the other specimens used in this study. To minimize the possible error associated with the selection of the threshold value, several trial threshold values were used for each specimen and an optimum value that includes most of the small pores without excessively

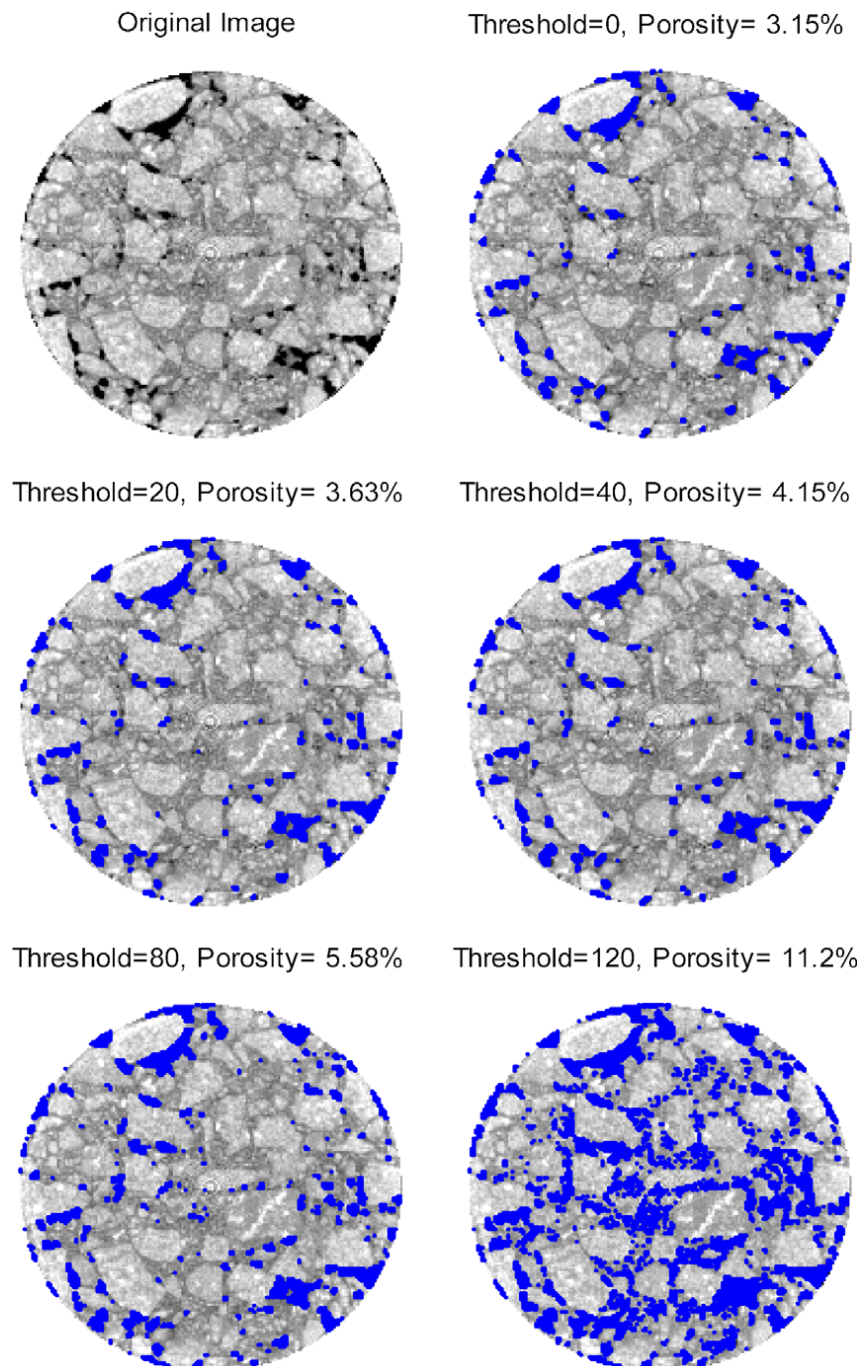


Fig. 11. Effect of threshold on porosity of specimen 25C75.

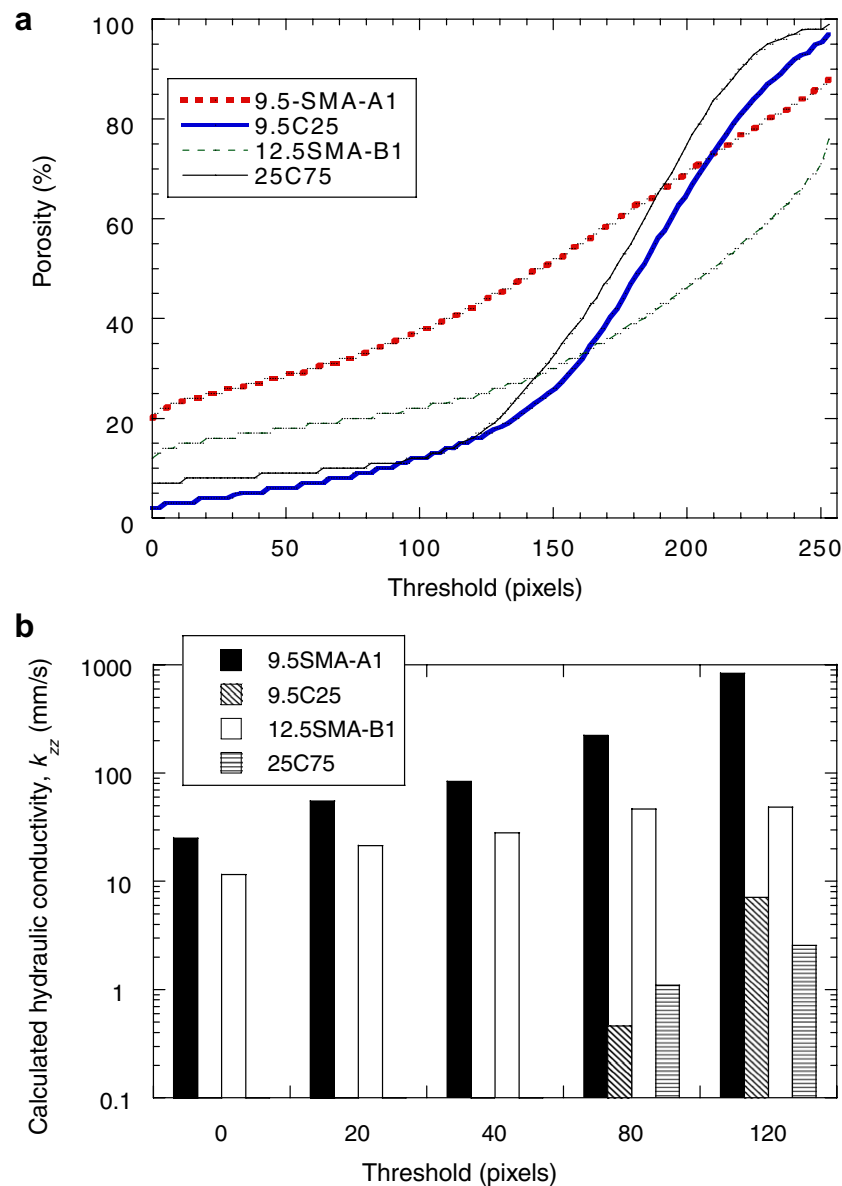


Fig. 12. Effect of threshold on porosity and hydraulic conductivity of asphalt specimens.

widening the larger pores was visually determined [19]. This may have caused slight deviations from the actual pore structure and the LB simulation results should be interpreted accordingly.

Fig. 12a shows the effect of the selected threshold on total porosity of four different hot mix asphalt specimens. Specimens 9.5C25 and 25C75 represent the typical characteristics exhibited by ideal pore structures, where the measured porosity sharply increases at a critical threshold value that clearly discriminates the pores from the solid nodes. For these two specimens, the selection of a threshold value is relatively simple, and it probably exists somewhere around 120. Conversely, the selection of a threshold value is more complicated for the two SMA specimens (9.5SMA-B1 and 12.5SMA-B1) as no clear deviation can be observed in the trend when porosity is plotted versus threshold. Fig. 12b shows the effect of threshold on simu-

lated hydraulic conductivities. It is clear that an increase in threshold value generates more openings in the pore structure and increases the hydraulic conductivity. According to authors' knowledge, there is no direct method for selecting the "correct" threshold during processing of the images. Thus, as mentioned above, a threshold value that includes most of the small pores without excessively widening the larger pores was visually determined and used during the LB simulations in the current study.

## 7. Conclusions

Methods were presented herein for conducting two- and three-dimensional simulations of flow of monophasic Newtonian incompressible fluid through simple geometries as well as complex geometries using the LB technique. Critical boundary conditions for LB flow simulations on two

geomaterials were presented, and the accuracy of LB model was verified against well-known analytical and theoretical solutions of permeability for simple geometries. An excellent agreement was observed between these solutions and the LB simulations for Stokes flow around a cylinder and flow in circular tubes. The percent error ranged from 0.1% to 2%. It was shown that the LB method is able to simulate fluid flow accurately even at very low resolutions (low number of lattice sites).

The performance of the three-dimensional LB model was further evaluated by comparing the simulation results to laboratory hydraulic conductivity tests conducted on compacted aggregates and asphalt specimens. X-ray CT and mathematical morphology-based techniques were used to analyze the pore structure of the specimens and these pore structures were input into the LB model. A very good agreement was observed between the model predictions and the laboratory measurements. The difference between the experimental results and the model was less for the asphalt mix specimens. This can be attributed to the fact that the applied hydraulic gradient was better controlled using specimen confinement during asphalt mix laboratory tests as compared to the aggregate tests. Sensitivity analyses was conducted to select the optimum threshold value in processing the X-ray CT images in order to accurately capture the pore structure and improve the computations of the hydraulic conductivity.

The presented model can accurately simulate 3D fluid flow in granular materials, such as aggregates and hot mix asphalt. The model is unique as X-ray CT was used to acquire real three-dimensional pore structures of the specimens, and boundary conditions specific to the phenomenon analyzed were implemented. Simulation of 3D fluid flow in these granular materials allows computation of certain inherent characteristics such as the hydraulic conductivity (permeability), and thus, may eliminate the need for costly and labor intensive laboratory measurements. Further, the computed flow variables can provide critical information for many other engineering problems. For example, computed flow velocities inside pore channel constrictions of an asphalt specimen can be used to calculate the pore pressures and shear stresses applied to the binder coats at the same constrictions. This may assist in the characterization of the asphalt mix resistance to fluid flow induced damage. The examples can be extended to environmental fluid flow problems such as contaminant transport through soils, oxygen sparging for soil remediation, and atmospheric particulate or gas flow through micropores of a geomembrane or geosynthetic clay liner used in landfill covers.

## Acknowledgements

The funding for this project was provided by US Department of Transportation, Federal Highway Administration (FHWA) through contract No. 03-X00-501 and the National Science Foundation funding through grants

CMS-0420494 and CMS-0315564. This support is gratefully acknowledged. The opinions expressed in this paper are solely those of the authors and do not necessarily reflect the opinions of the FHWA. Authors would also like to thank Dr. Nick Martys of the National Institute of Science and Technology (NIST) for his valuable suggestions on the LB model.

## References

- [1] Adler PM, Jacquin CG, Quiblier JA. Flow in simulated porous media. *Int J Multiphase Flow* 1990;16:691–712.
- [2] ASTM D 2434. Standard Test Method for Permeability of Granular Soils (Constant Head). West Conshohocken, Pennsylvania, USA: American Society for Testing and Materials.
- [3] AASHTO T 166. Standard Test Method for Bulk Specific Gravity of Compacted Asphalt Mixtures Using Saturated Surface-Dry Specimens. American Association of State Highway and Transportation Officials.
- [4] AASHTO T 209-99. Standard Test Method for Theoretical Maximum Specific Gravity and Density of Bituminous Paving Mixtures. American Association of State Highway and Transportation Officials.
- [5] Al-Omari A, Masad E. Three dimensional simulation of fluid flow in X-ray CT images of porous media. *Int J Numer Anal Methods Geomech* 2004;28:1327–60.
- [6] Aydilek AH, Kutay ME. Development of an innovative computer controlled water deairing system for hydraulic testing of geosynthetics. *J Test Eval*, ASTM 2004;32(2):161–6.
- [7] Bear J. Dynamics of fluids in porous media. New York, NY: American Elsevier Publishing Co.; 1990.
- [8] Carman PC. Flow of gases through porous media. New York, NY: Academic Press; 1956.
- [9] Chen S, Doolen GD. Lattice Boltzmann method for fluid flows. *Annual Rev Fluid Mech* 2001;30:329–64.
- [10] Chin J, Boek ES, Covaney PV. Lattice Boltzmann simulation of the flow of binary immiscible fluids with different viscosities using the Shan–Chen microscopic interaction model. *Philos Trans R Soc Lond* 2002;547:58.
- [11] Chopard B, Droz M. Cellular automata modeling of physical systems. In: Godreche Claude, editor. Collection Alea-Saclay: monographs and texts in statistical physics. Cambridge, UK: Cambridge University Press; 1998.
- [12] Duarte JA, Shaimi MS, Carvalho JM. Dynamic permeability of porous media by cellular automata. *J Phys II*, France 1992;1(5).
- [13] Dullien FAL. Porous media: fluid transport and pore structure. San Diego, California: Academic Press; 1992. 574 p..
- [14] Hazi G. Accuracy of lattice Boltzmann based on analytical solutions. *Phys Rev E* 2003;67:056705-1–5-5.
- [15] He X, Luo L. Theory of lattice Boltzmann method: From the Boltzmann equation to the lattice Boltzmann. *Phys Rev E* 1997;56:6811–7.
- [16] Kandhai D, Vidal DJE, Hoekstra AG, Hoefsloot H, Iedema P, Sloot PMA. Lattice Boltzmann and finite element simulations of fluid flow in a SMRX static mixer reactor. *Int J Numer Methods Fluids* 1999;31(6):1019.
- [17] Kozeny J. Ueber Kapillare Leitung des Wassers im Boden. Wien, Akad. Wiss.; 1927.
- [18] Kutay ME. Modeling moisture transport in asphalt pavements. PhD dissertation, University of Maryland, College Park, MD, 2005.
- [19] Kutay ME, Aydilek AH. Lattice Boltzmann in modeling fluid flow through asphalt concrete. *Environmental Geotechnics Report 05-2*, University of Maryland, College Park, MD, 2005, 284 p.
- [20] Maier RS, Bernard RS, Grunau DW. Boundary conditions for the lattice Boltzmann method. *Phys Fluids* 1996;8(7):1788–801.



- [21] Maier R, Kroll D, Kutsovsky Y, Davis HT, Bernard R. Simulation of flow through bead packs using the lattice Boltzmann method. AHPARC Preprint 97-034, Univ. of Minnesota.; 1997.
- [22] Martys NS, Hagedorn JG, Devaney JE. Pore scale modeling of fluid transport using discrete Boltzmann methods. In: Proceedings of materials science of concrete, Special Volume: Ion and mass transport in cement-based materials, Toronto, Canada, 2001. p. 239–52.
- [23] Masad E, Muhunthan B, Martys N. Simulation of fluid flow and permeability in cohesionless soils. *Water Resour Res* 2000;36:851–64.
- [24] Mitchell JK. Fundamentals of soil behavior. 2nd ed. New York: John Wiley and Sons, Inc.; 1993.
- [25] McNamara G, Zanetti G. Use of the Boltzmann equation to simulate lattice-gas automata. *Phys Rev Lett* 1988;61:2332–5.
- [26] Roberts FL, Kandhal PS, Brown ER, Lee D, Kennedy T. Hot mix asphalt materials, mixture design and construction. Maryland: NAPA Education Foundation; 1996.
- [27] Rothman DH, Zaleski S. Lattice-gas model of phase separation: interfaces, phase transitions, and multiphase flow. *Rev Mod Phys* 1998;66(4):1471–9.
- [28] Scheidegger AE. The physics of flow through porous media. Toronto: University of Toronto Press; 1957.
- [29] Succi S. The lattice Boltzmann equation: for fluid dynamics and beyond. Numerical mathematics and scientific computation series. Oxford-New York: Oxford University Press; 2001.
- [30] Wannier GH. A contribution to the hydrodynamics of lubrication. *Quart Appl Math* 1950;8(1):1–32.
- [31] Walsh JB, Brace WF. The effect of pressure in porosity and the transport properties of rock. *J Geophys Res* 1984;89(B11): 9425–31.
- [32] Wolf-Gladrow DA. Lattice-gas cellular automata and lattice Boltzmann models: an introduction. Berlin: Springer; 2000.
- [33] Yu D, Mei R, Luo LS, Shyy W. Viscous flow computations with the method of lattice Boltzmann equation. *Prog Aerospace Sci* 2003;39:329–67.
- [34] Ziegler DP. Boundary conditions for lattice Boltzmann simulations. *J Statist Phys* 1993;71(1171).
- [35] Zou QS, He XY. On pressure and velocity boundary conditions for the lattice Boltzmann BGK model. *Phys Fluids* 1997;9(6):1591–8.